Electronic Supplementary Material (ESI) for RSC Advances.

Deposition of platinum on boron doped TiO_2/Ti nanotube arrays as an efficient and stable photocatalyst for hydrogen generation from water splitting

Mengjia Sun,[a] Yanli Jiang,[*b] Mei Tian,[*ab] Huijun Yan,[b] Ran Liu[b] and Lijuan Yang[b]

a. School of Chemistry and Materials Science,Heilongjiang University,Harbin 150080, P.R.China

b. Department of Chemistry, Harbin University, Harbin, 150086, P.R.China

† Email address: jylzhl@163.com; shl913@vip.sina.com.

Supporting Informantion

1. Experimental section

1.1. Materials

$Ni(NO_3)_2$, ethylene glycol (EG), Sodium borohydride ($NaBH_4$) were purchased from Tianjin Kermel Chemical Reagent Co. Ltd. $Co(NO_3)_2 \cdot 6H_2O$, P-nitrophenol ($C_6H_5NO_3$) and 2-methylimidazole were purchased from Aladdin Ltd. $CO(NH_2)_2$, methanol were purchased from Tianjin GuangFu Fine Chemical Research Institute, and all were used without further purification.

1.2. The preparation for $Ni(OH)_2$ nanosheets

The $Ni(OH)_2$ nanosheets were prepared by a hydrothermal procedure reported by Sun et al.[1] Briefly, 0.524 g of $Ni(NO_3)_2 \cdot 6H_2O$ and 0.216g $CO(NH_2)_2$ were dissolved in a 40 mL mixture of 16 mL deionized water and 24 mL ethylene glycol. After 20 min of vigorous stirring at ambient temperature, the as-prepared solution was transferred into Teflon-lined autoclave. The autoclave was sealed and heated up to 140 ^oC for 4 h. Afterward the system was allowed to cool down to room temperature, the light green products were collected by centrifugation and washing several times with deionized water and ethanol, then dried at 60 ^oC overnight for further use.

1.3. Synthesis of ZIF-67/$Ni(OH)_2$

The ZIF-67/$Ni(OH)_2$ were prepared in aqueous solution at room temperature. Typically, $Ni(OH)_2$ (0.151 g) was dispersed in the binary mixture of 10mL methanol and 10 mL ethanol. $Co(NO_3)_2 \cdot 6H_2O$ (0.146 g) was dissolved in other binary mixture of 4 mL methanol and 4 mL ethanol. 2-methylimidazole (0.164 g) was dissolved in another mixture of 4 mL methanol and 4 mL ethanol. After $Co(NO_3)_2 \cdot 6H_2O$ solution was added into $Ni(OH)_2$ solution with the assistance of sonication, the 2-methylimidazole solution was quickly poured into the pink solution. The reaction was performed for 24 h at room temperature. The precipitate was isolated from the solution by centrifugation at 4000 rpm for 5 min, and rinsed with methanol for three times, and finally dried at 60^oC. The final product was designated as ZN-1. When the mole ratio of

$Co(NO_3)_2 \cdot 6H_2O$ and $Ni(OH)_2$ were 0.5/3, 2/3, and 3/3, the final products were designated as ZN-0.5, ZN-2, ZN-3, respectively.

1.4. Synthesis 2-D Ni_3N-Co_3N hybrids

The as-prepared ZIF-67/$Ni(OH)_2$ precursors were loaded in porcelain boats, and then heated to 350 ^oC for 3 h with a heating rate of 2 ^oC min^{-1} under NH_3 atmosphere and then cooled to room temperature, and Ni_3N-Co_3N was obtained. ZN-1 was also calcined at 300, 400, and 450 ^oC under a NH_3 atmosphere to tune the structures of the samples. The samples were named ZN-1-300, ZN-1-400, and ZN-1-450 respectively.

1.5. Characterization

Scanning electron microscopy (SEM, Hitachi SU-70) was used to characterize the morphologies, and Transmission electron microscopy (TEM, JEM-2100) was further detect the crystalline structures. Powder X-ray diffraction (XRD) patterns were obtained on a Bruker D8 X-ray diffractometer (Cu Kα radiation, λ = 1.5406 Å). Raman spectra was collected by using a Jobin Yvon HR 800 micro-Raman spectrometer with a 457.9 nm laser as excitation source. An X-ray photoelectron spectra (XPS) was conducted on VG ESCALAB MK II using an Mg Ka (1253.6 eV) achromatic X-ray radiation. N_2 adsorption-desorption experiments were performed on a Micromeritics Tristar II) instrument. Fourier transform infrared spectrum was measured from a NICOLETIS10 spectrometer.

1.6. Catalytic hydrogenation reaction of p-nitrophenol

Catalytic hydrogenation reaction of p-NP in the presence of excess $NaBH_4$ was conducted in aqueous solution atmospheric pressure and 15^{o}C, 25^{o}C, 35^{o}C, 45^{o}C. In a typical experiment, the catalytic hydrogenation reaction of PNP to PAP was conducted in a 250 mL three-necked round-bottomed flask with 0.3 mM 80 mL PNP aqueous solution, and the solution was mechanically stirred with impeller. After 0.4 M 10 mL freshly prepared $NaBH_4$ aqueous solution was injected into 80 mL of PNP solution, the color of solution changed from light yellow to bright yellow.[2] Subsequently, 6 mL dispersed catalyst (3 mg)

solution was added and the solution was stirred. The reaction progress was evaluated by taking a small portion of the reaction mixture every minute and measuring the UV–vis spectra on UV-1600/1800B. After the reaction, the catalyst can be easily removed from the solution phase under an external magnetic field, washed with water and then reused 10 times in succession under the same reaction conditions.

1.7. TOF: molecules of 4-NP converted per quality of Ni_3N-Co_3N per second.

$$TOF_{Ni_3N-Co_3N} = \frac{CVN_A}{mt}$$
$$= \frac{0.3mM \times 10^{-3} \times 80mL \times 10^{-3} \times 6.02 \times 10^{23}}{3mg \times 10^{-3} \times 239s}$$
$$= 2.02 \times 10^{19}\ \text{molecule}\ g^{-1}s^{-1}$$

$$TOF_{Ni_3N} = \frac{CVN_A}{mt}$$
$$= \frac{0.3mM \times 10^{-3} \times 80mL \times 10^{-3} \times 6.02 \times 10^{23}}{3mg \times 10^{-3} \times 492s}$$
$$= 9.79 \times 10^{18}\ \text{molecule}\ g^{-1}s^{-1}$$

$$TOF_{ZIF-67-350} = \frac{CVN_A}{mt}$$
$$= \frac{0.3mM \times 10^{-3} \times 80mL \times 10^{-3} \times 6.02 \times 10^{23}}{3mg \times 10^{-3} \times 1944s}$$
$$= 2.48 \times 10^{18}\ \text{molecule}\ g^{-1}s^{-1}$$

C: Concentration of PNP, V: Volume of PNP, m: Quality of catalyst, t: Reaction time, $N_{A:}\ 6.02 \times 10^{23}$.

1.8. Electrochemical measurements

The electrochemical measurement was performed with a BAS100B electrochemical workstation in a typical three-electrode system at ambient temperature, with Ag/AgCl electrode (saturated KCl-filled) as reference

electrode, glassy carbon electrode (GCE, 0.07065 $cm^{-2}$of area) as work electrode and graphite rod electrode as counter electrode, and 1 M KOH was used as electrolyte. All the potentials recorded with respect to the reversible hydrogen electrode (RHE) on the basis of the Nernst equation without iR correction: $E_{vsRHE} = E_{vsAg/AgCl} + 0.207 + 0.059$ pH.[3] Catalyst ink was typically made by dispersing 5 mg of catalyst and 0.5 mg carbon black in 1 mL ethanol/water mixture (v/v=1:1). Then a total of 10 μL of the catalysis slurry was dropped onto the surface of the bare GCE. The activity of Ni_3N-Co_3N toward the HER was examined by linear sweep voltammetry (LSV) with a scan rate of $5mVs^{-1}$. The stability test was obtained by cyclic voltammetry (CV) scanning of 2000 and 4000 cycles with a scan rate of $100mVs^{-1}$.

Figure captions

Figure S1. a-d) SEM images of ZN-0.5, ZN-1, ZN-2, ZN-3. Inset: SEM images of ZN-1, ZN-2, ZN-3. e-f) TEM images of ZN-1. g-h) higher magnified TEM images of ZN-1. i-l) photos of $Ni(OH)_2$, ZN-1, ZIF-67, ZN-1-350.

Figure S2. N_2 adsorption-desorption isotherms of (a) ZIF-67, ZN-1, $Ni(OH)_2$ and b) Ni_3N-Co_3N (ZN-1-350).

Figure S3. a-b) Raman spectras of the Ni_3N-Co_3N, Ni_3N, ZIF-67, ZIF-67 after calcination in NH_3 (ZIF-67-350).

Figure S4. a-b) SEM images of ZN-1-350, $Ni(OH)_2$-350.

Figure S5. XPS spectra of ZN-1-350. a) wide scan spectrum and the high-resolution spectra of b) Ni 2p c) Co 2p d) N1s.

Figure S6. a) Co XPS spectra of ZIF-67-350. b) Co XPS spectra of ZIF-67. c) Ni XPS spectra of $Ni(OH)_2$-350. d) N XPS spectra of $Ni(OH)_2$-350.

Figure S7. a) XRD pattern of as synthesized ZIF-67 and ZIF-67-350. b) SEM image of ZIF-67-350. c-d) XRD pattern and SEM image of 20mgZIF-67/10mg$Ni(OH)_2$-350. e-f) XRD pattern and SEM image of 20mg $Ni(OH)_2$/10mg $Ni(OH)_2$-350.

Figure S8. a) XRD pattern of the ZN-1-300, ZIF-67. b) XRD pattern of the as synthesized ZN-1-400. c-d) SEM images of ZN-1-300, ZN-1-400.

Figure S9. a) UV-vis absorption spectra of p-NP catalyzed by Ni_3N catalyst at 25 ^oC. b) UV-vis absorption spectra of p-NP catalyzed by ZIF-67-350 catalyst at 25^oC.

Figure S10. a-c) UV–vis absorption spectra of p-NP catalyzed by Ni_3N-Co_3N catalyst at 15^oC, 35^oC, 45^oC.

Figure S11. a-b) UV–vis absorption spectra of p-NP catalyzed by ZN-2-350, ZN-0.5-350. c) Pseudo-first-order plot of ln (C/C_0) against reaction time on ZN-0.5-350, ZN-1-350 and ZN-2-350 at 25^oC. d) k_{app} of different catalysts at 25^oC.

Figure S12. Magnetic hysteresis loop of Ni_3N-Co_3N catalyst at the temperature of

300K. The inset shows the enlargement of M–H loop at low magnetic field and the illustration of magnetic separation by an external magnet.

Figure S13. a) Polarization curves for ZIF-67-350, $Ni(OH)_2$-350, ZN-1-350, and Pt/C in 1M KOH with a scan rate of 5 mVs^{-1}. b) Tafel plots for ZIF-67-350, $Ni(OH)_2$-350, ZN-1-350 and Pt/C. c) Nyquist plots of ZIF-67-350, $Ni(OH)_2$-350, and ZN-1-350. The inset in (c) is the Nyquist plots for the high frequency region. d) Polarization data for the ZN-1-350 sample in 1M KOH initially and after 2000, and 4000 CV sweeps between -1000 mV and -1800 mV vs RHE. The inset in (d) is the time dependence of the current density for ZN-1-350 under the temporal evolution of the potential required to maintain 10 mA cm^{-2} for 24h.

Figure S14. a-c) CVs for ZIF-67-350, $Ni(OH)_2$-350, ZN-1-350 with different rates from 40 to 200 mVs^{-1}. The inset in (a-c) is the capacitive current at 0.21 V as a function of scan rate for ZIF-67-350(j_0= ja-jc), $Ni(OH)_2$-350(j_0= ja-jc), ZN-1-350(j_0= ja-jc). d) Exchange current density of ZIF-67-350, $Ni(OH)_2$-350, ZN-1-350 composites.

Figure S15. a) Polarization data for ZIF-67/$Ni(OH)_2$ calcined in different temperatures. b) Polarization data for different ratio ZIF-67/$Ni(OH)_2$ calcined at 350^{o}C. c) Tafel plots for ZN-1-300, ZN-1-350, ZN-1-400, ZN-1-450. d) Tafel plots for ZN-0.5-350, ZN-1-350, ZN-2-350, ZN-3-350.

Figure S16. a) CVs of $Ni(OH)_2$-350, ZIF-67-350, ZN-1-350 in 1 M PBS with a scan rate of 50 mVs^{-1}. b) Calculated TOF for $Ni(OH)_2$-350, ZIF-67-350, ZN-1-350 in 1 M KOH.

Table S1 The samples and their corresponding synthesis parameters.

Table S2 Rate constants of the reduction of p-nitrophenol to p-aminophenol by metal catalysts.

Table S3 The performance of different catalysts for HER.

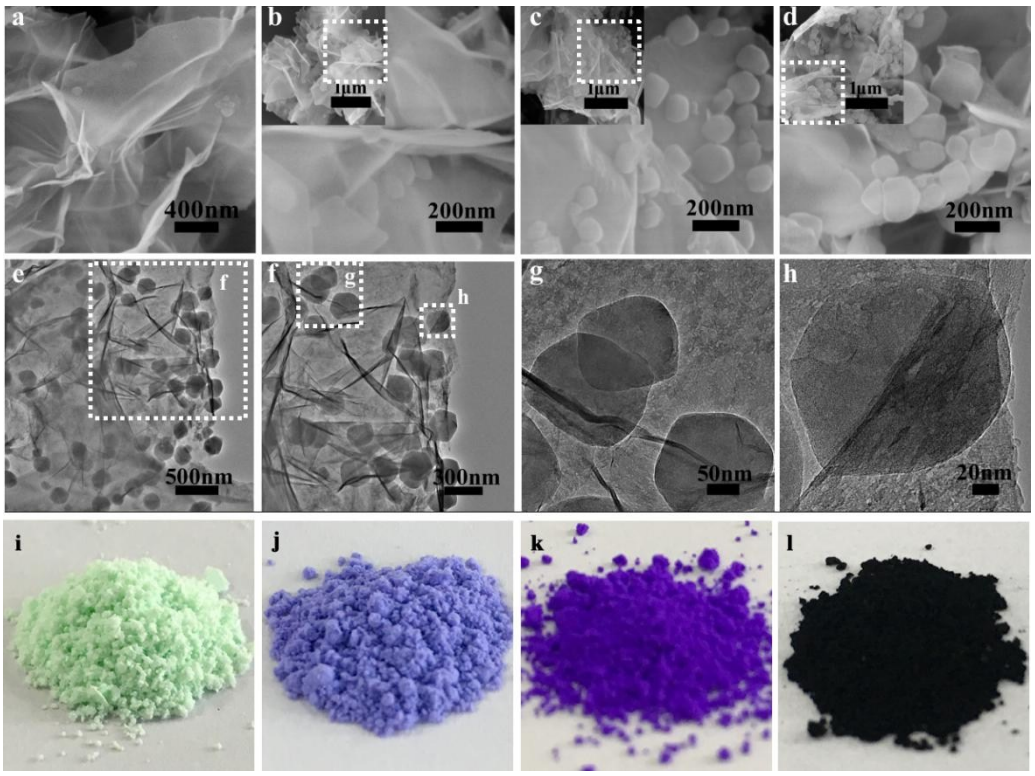

Figure S1. a-d) SEM images of ZN-0.5, ZN-1, ZN-2, ZN-3. Inset: SEM images of ZN-1, ZN-2, ZN-3. e-f) TEM images of ZN-1. g-h) higher magnified TEM images of ZN-1. i-l) photos of $Ni(OH)_2$, ZN-1, ZIF-67, ZN-1-350.

As shown in Figure S1a-d, the ZIF-67 polyhedrals were integrated on the surface of the $Ni(OH)_2$ nanosheets. Also, with the increase in the mole ratio of cobalt and nickel, the polyhedrons on the nanosheets also gradually increased.

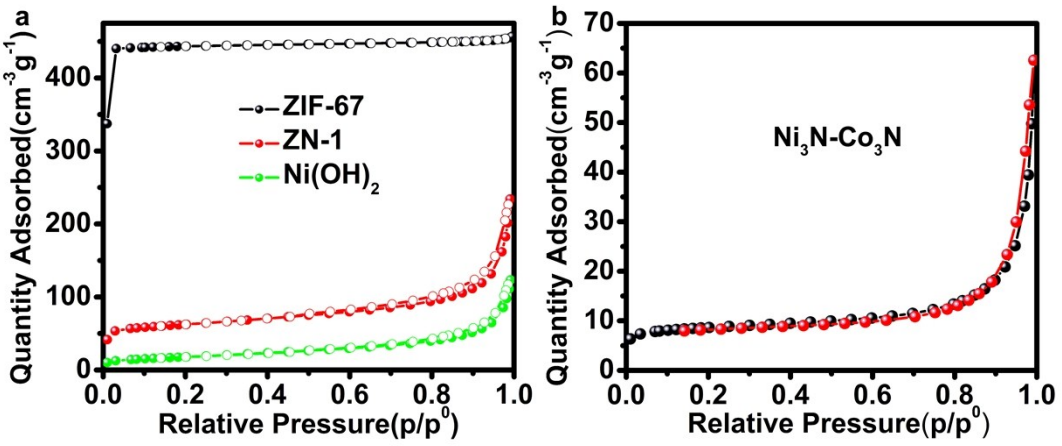

Figure S2. N_2 adsorption-desorption isotherms of a) ZIF-67, ZN-1, $Ni(OH)_2$ and b) Ni_3N-Co_3N (ZN-1-350).

The N_2 adsorption/desorption test shows that the S_{BET} values of ZN-1 (216.11 $m^{-2}g^{-1}$) is between $Ni(OH)_2$ (64.14 $m^{-2}g^{-1}$) and ZIF-67 (1507.83 $m^{-2}g^{-1}$), indicating that the combination of ZIF-67 and $Ni(OH)_2$ has low specific surface area. The curve shows a strong N_2 adsorption in the low pressure region and a distinct hysteresis in the high pressure region, implying coexistence of meso-/macropores and micropores. This clearly demonstrates the successful combination of $Ni(OH)_2$ and ZIF-67.[4] Figure S2b is the N_2 adsorption-desorption isotherm of Ni_3N-Co_3N (ZN-1-350) hybrids. The specific surface area of Ni_3N-Co_3N is 30.02 m^2 g^{-1}.

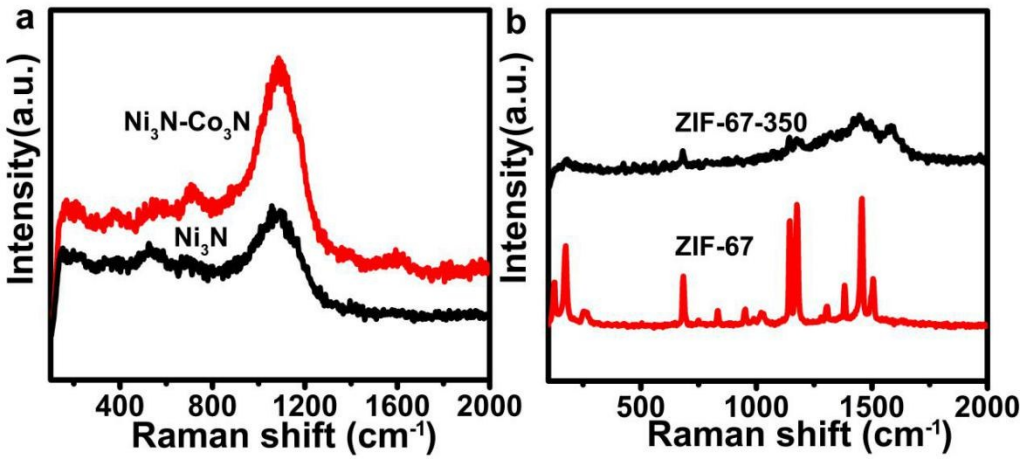

Figure S3. a-b) Raman spectras of the Ni_3N-Co_3N, Ni_3N, ZIF-67, ZIF-67 after calcination in NH_3 (ZIF-67-350).

In Figure S3a, the obvious peak located at 702 cm^{-1} is identified for metal-N bond in the spectrum of Ni_3N-Co_3N.[5] The peaks corresponding to metal-O can also be observed at 1110 cm^{-1} and 521cm^{-1}, which should be ascribed the surface oxidation of nitrides under air.[6] The Raman spectrum is also similar to Ni_3N derived from $Ni(OH)_2$, further indicating the formation of nitrides in ZN-1-350. In Figure S3b, it can be clearly observed that ZIF-67 did not change its peak position before and after calcination, which reflected the role of $Ni(OH)_2$ in promoting transformation.

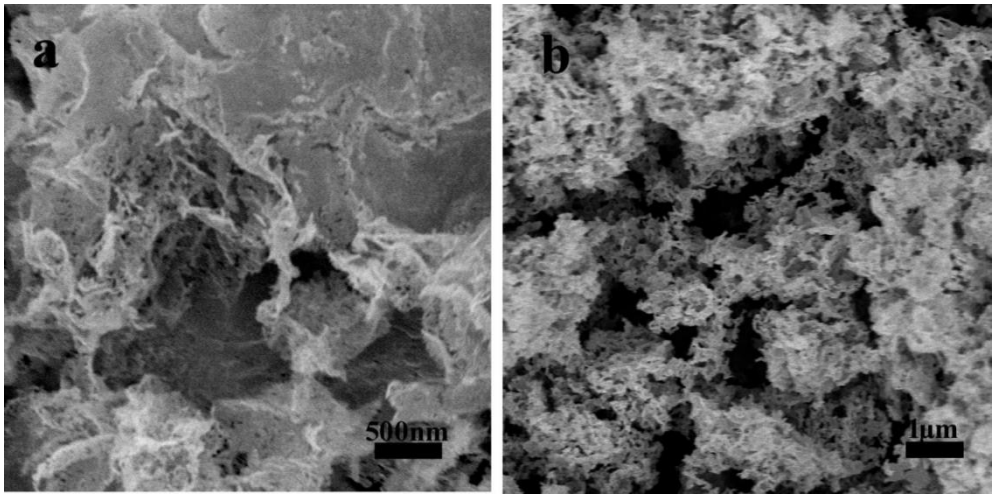

Figure S4. a-b) SEM images of ZN-1-350, $Ni(OH)_2$-350.

Figure S4a shows the SEM image of ZN-1-350 from calcining ZIF-67/$Ni(OH)_2$ precursor under NH_3 at 350°C 3h. The samples shows well sheet-like structure, being consistent with the TEM result. Figure S4b shows SEM image of Ni_3N derived from $Ni(OH)_2$ after calcination in NH_3 at 350^{o}C for 3h. We can see that the morphology of $Ni(OH)_2$ after calcination was destroyed. So, it is obvious that the ZIF-67 can act as a "baffle" to prevent the aggregation of 2-D $Ni(OH)_2$ during the nitridation.

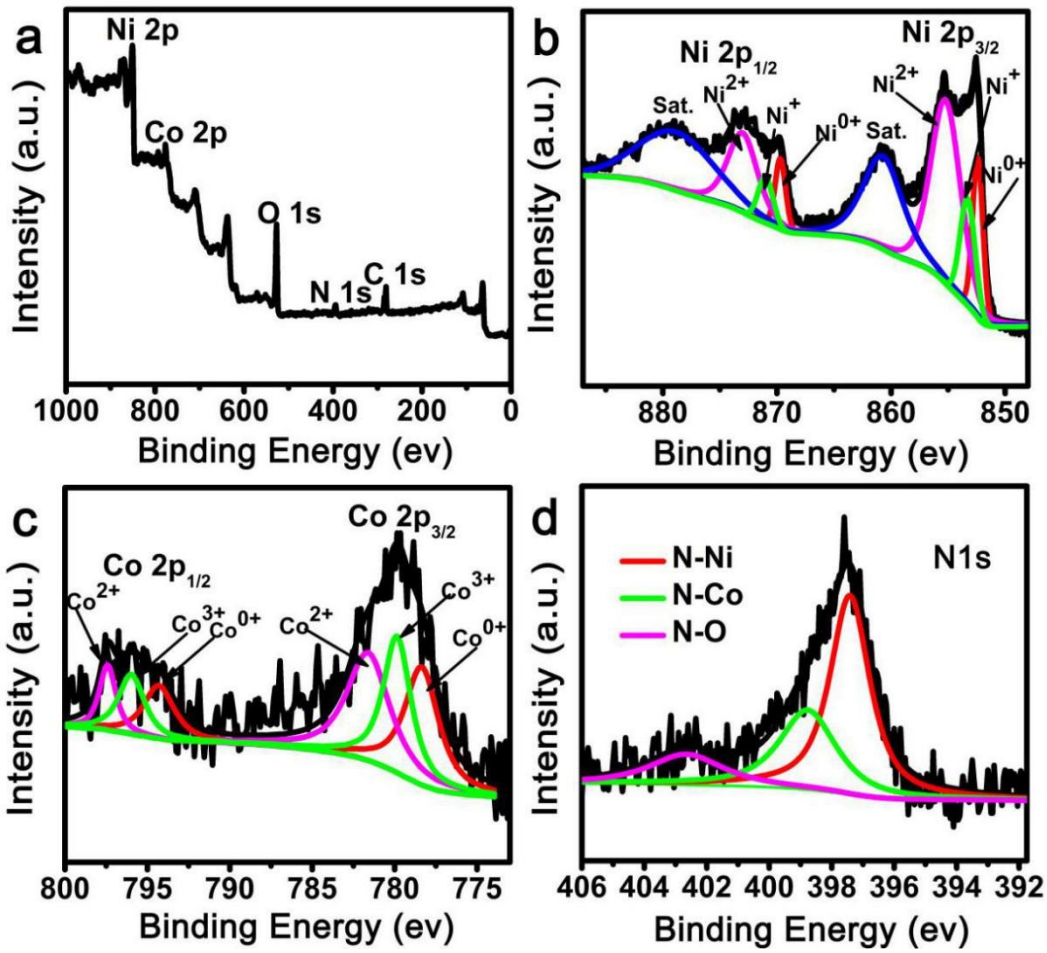

Figure S5. XPS spectra of ZN-1-350. a) wide scan spectrum and the high-resolution spectra of b) Ni 2p c) Co 2p d) N1s

The wide XPS spectra of Ni_3N-Co_3N nanosheets was shown in Figure S5a, which indicates that Ni, Co, C, N, O elements were observed. XPS analysis indicates that Co exists on the surface of the sample after calcination. According to previous literature, the peaks located at 853.2 eV, 871 eV can be ascribed to Ni $2p_{3/2}$, and Ni $2p_{1/2}$ in Ni_3N,[7] and the peaks located at 852.4 eV and 869.7 eV can be assigned to Ni^{0+}.[8] Meanwhile, the peaks at 855.2 eV, 860.7 eV, 873 eV and 878.8 eV can be ascribed to Ni $2p_{3/2}$, Ni $2p_{1/2}$ and Ni satellite peaks in NiO,[8,9] which demonstrates the exsitence of surface oxidation in Ni_3N nanosheets. However, the NiO still couldn't be detected by XRD, giving the evidence that the major phase was Ni_3N with some surface oxidized layers. Compared to Ni 2p in pure nickel nitride, the overall peak shifts toward low binding energy (Figure S6c). The Co 2p XPS spectrum (Figure S5c)

displays two peaks at 778.3 and 794.3eV corresponding to the $2p_{3/2}$ and $2p_{1/2}$ peaks of metal cobalt in Co_3N.[7,10] Deconvolution of the spectrum reveals the existence of Co^{3+} with the spin-orbit doublets at 779.8 and 795.9 eV, which can be ascribed to Co-N.[10,11] Co^{2+} with the spin-orbit doublets is at 781.6 and 797.4 eV.[12] This is due to the surface oxidization of metallic Co in the Ni_3N-Co_3N.[12] However, the cobalt in pure ZIF-67-350 is only present in the Co^{2+}, as shown in Figure S6a, which is the same as the existing form of cobalt in pure ZIF-67 (Figure S6b). This further proves that the presence of $Ni(OH)_2$ accelerates the decomposition of ZIF-67. The binding energy of N 1s in Ni_3N-Co_3N is 397.4, 398.7, and 402.5, which are the peaks of N-Ni,[13] N-Co,[14] and N-O.[15]

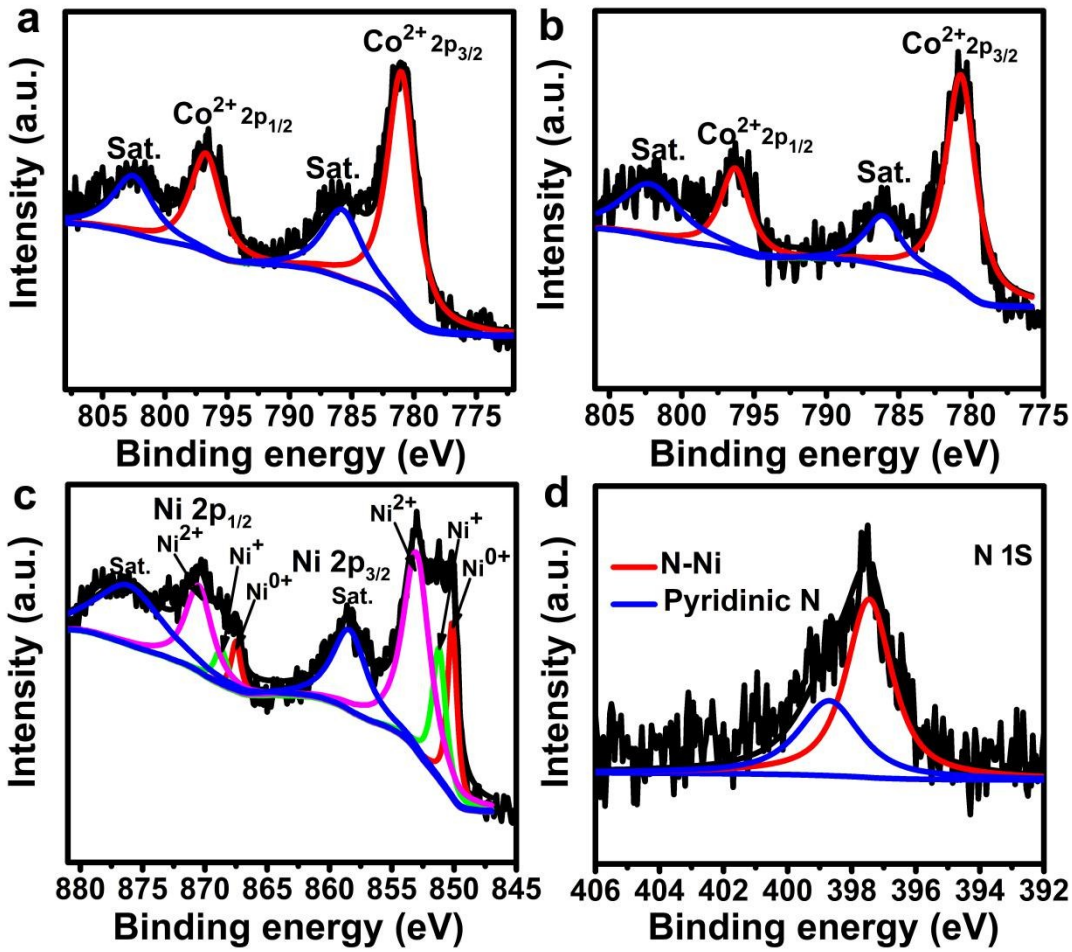

Figure S6. a) Co XPS spectra of ZIF-67-350. b) Co XPS spectra of ZIF-67. c) Ni XPS spectra of $Ni(OH)_2$-350. d) N XPS spectra of $Ni(OH)_2$-350.

As shown in Figure S6a, the fitting data reveal two peaks ($2p_{3/2}$ peak at 781.0 and $2p_{1/2}$ peak at 796.7 eV) corresponding to Co^{2+}.[12] In Figure S6b, it can be seen that main peaks of Co $2p_{3/2}$ and Co$2p_{1/2}$ located at binding energies of 779.6 and 795.1 eV, respectively.[12] As shown in the Figure S6c, the nickel in Ni_3N can also be divided into the peaks corresponding to Ni^{0+}, Ni^{+}, Ni^{2+}. As shown in the Figure S6d, N can only be divided into two peaks, corresponding to Ni-N and pyridinic N.[13]

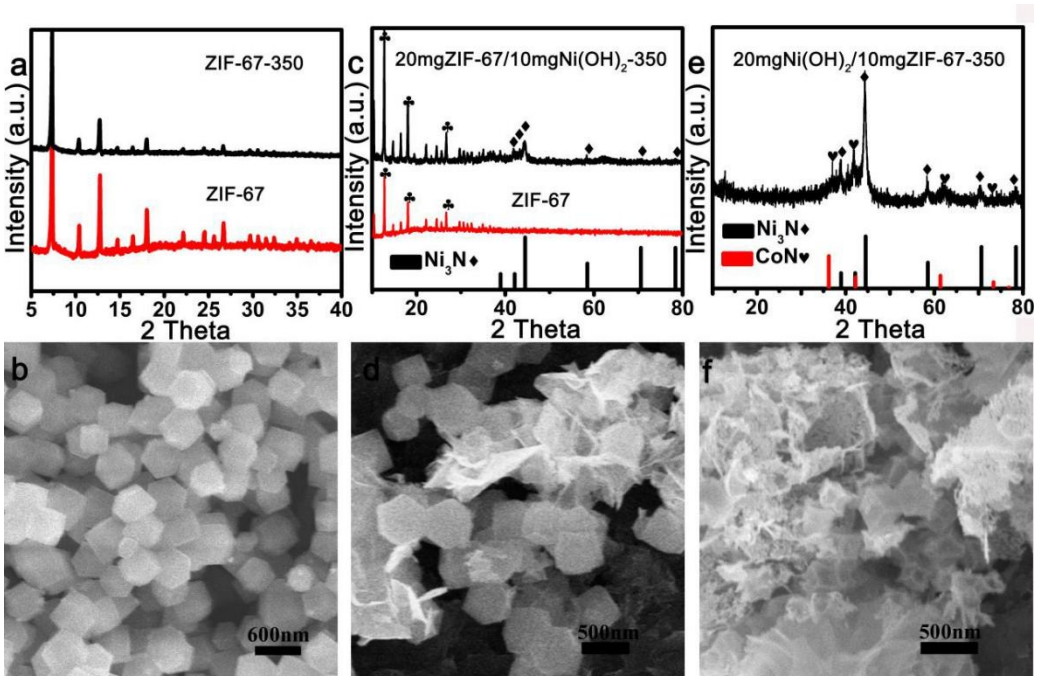

Figure S7. a) XRD pattern of the as synthesized ZIF-67 and ZIF-67-350. b) SEM image of ZIF-67-350. c-d) XRD pattern and SEM image of 20mg ZIF-67/10mg$Ni(OH)_2$-350. e-f) XRD pattern and SEM image of 20mg $Ni(OH)_2$/10mg $Ni(OH)_2$-350.

Figure S7 gives the XRD pattern of ZIF-67 and ZIF-67-350. We can see that two samples show similar peaks. The SEM image of ZIF-67-350 have shown uniform polyhedron morphology, being similar to that of ZIF-67. The result indicates little change of ZIF-67 after calcination at 350 ^{o}C, as well as the promoted role of Ni species on the nitridation of ZIF-67.

To further verify the role of $Ni(OH)_2$, the pre-synthesized ZIF-67 and $Ni(OH)_2$ are physically mixed with different mass ratio. It is obvious that the conversion of

ZIF-67 can be accelerated with the increase of amount of $Ni(OH)_2$. For the sample composed of 20 mg ZIF-67 and 10 mg $Ni(OH)_2$, the ZIF-67 retains its morphology and structure after calcination under NH_3 for 3h. Nevertheless, the conversion of ZIF-67 into nitrides can be observed with the changing of the mass ratio of $Ni(OH)_2$ and ZIF-67 to 20mg/10mg. We can observe the presence of shrink polyhedron in SEM images (Figure S7f) and obvious diffraction of CoN. We speculated that $Ni(OH)_2$ in ZIF-67/$Ni(OH)_2$ will predominantly react with NH_3 to give Ni_3N. The Ni_3N may act as "active center" to promote the reaction of ZIF-67 with NH_3. The promoted action may be similar to well-known "seed-growth" process, in which the pre-presented seeds (Ag, Au etc.) can make more easily reduction of post-added metal salts around the "seeds" [Ref. S1].

Ref. S1:

a) Y. Xia, Y. Xiong, B. Lim, and SE. Skrabalak, *Angew. Chem. Int. Ed.* , 2009, **48**, 60.

b) K. D. Gilroy, A. Ruditskiy, H. C. Peng, D. Qin, and Y. Xia, *Chem. Rev.* , 2016, **116**, 10414.

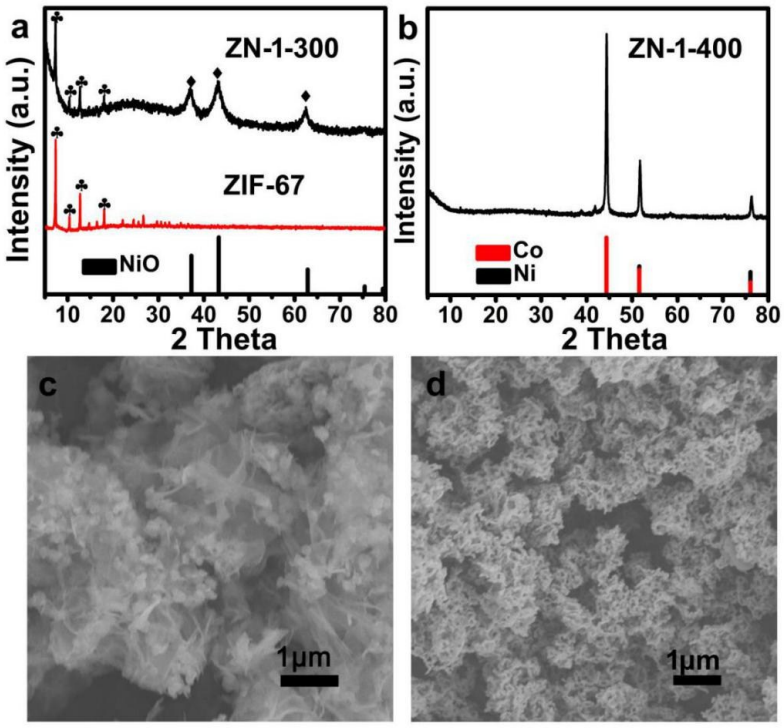

Figure S8. a) XRD pattern of the ZN-1-300，ZIF-67; b) XRD pattern of the as synthesized ZN-1-400. c-d) SEM images of ZN-1-300, ZN-1-400.

From Figure S8a, we can see that ZN-1-300 consists of NiO and ZIF-67. The SEM image shows the presence of polyhedron located on nanosheet (Figure S8c). The test indicates that low calcination temperature can not convert the precursor into 2-D nitride hybrids. However, as the temperature rises to 400°C, the ZIF-67 can be decomposed and no polyhedron can be observed (Figure S8b, 8d). Thus, we selected the 350 °C as most suitable calcination temperature to obtain 2-D Ni_3N-Co_3N hybrids.

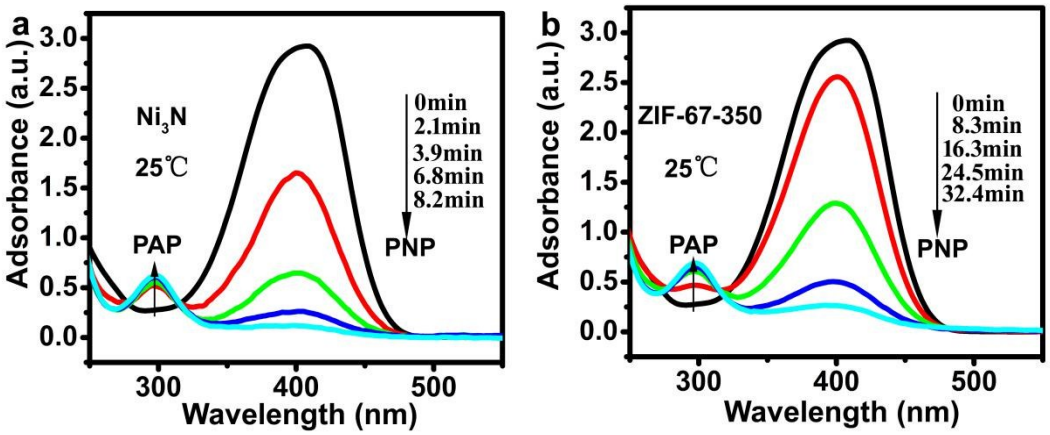

Figure S9. a) UV-vis absorption spectra of p-NP catalyzed by Ni_3N catalyst at 25 °C. b) UV-vis absorption spectra of p-NP catalyzed by ZIF-67-350 catalyst at 25 °C.

Figure S9a is the UV–vis absorption spectra of p-NP catalyzed by Ni_3N. Figure S9b is the UV–vis absorption spectra of p-NP catalyzed by ZIF-67-350. The conversion of p-NP to p-AP is complete in 8.2 min on Ni_3N, and 32.4 min on ZIF-67-350. In contrast, the reduction is completed within 3.28 min on 2-D Ni_3N-Co_3N in same experimental conditions (Figure 3e). The comparison further indicates that ZN-1-350 is more active than Ni_3N and ZIF-67-350.

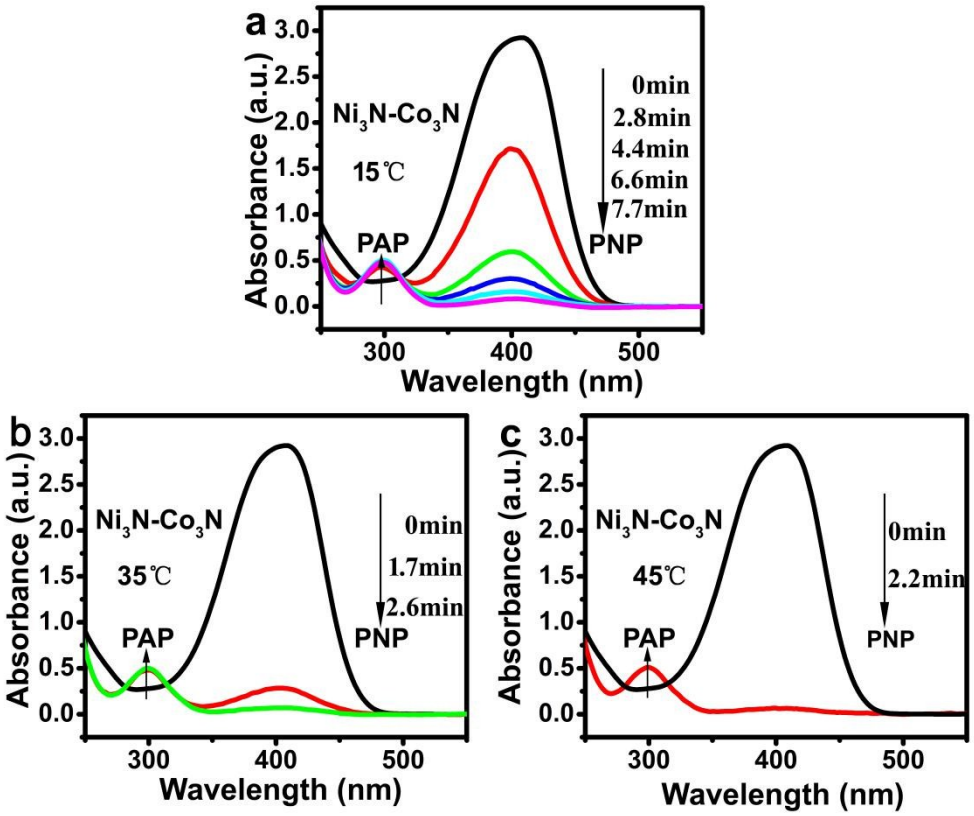

Figure S10. a-c) UV–vis absorption spectra of p-NP catalyzed by Ni_3N-Co_3N catalyst at 15°C, 35°C, 45°C.

The 2-D Ni_3N-Co_3N was chosen as typical sample to evaluate the effect of temperature on the reduction of p-NP since the reaction temperature is one of essential factors for the reduction of p-NP. The catalytic hydrogenation of p-NP over Ni_3N-Co_3N catalyst was carried out at four different temperatures ranging from 15 °C to 45 °C with an excessive amount of $NaBH_4$ under ambient pressure. As shown in Figures S10a-c, the reaction time is further reduced as the reaction temperature increases. When the reaction temperature is 45°C, the time required only takes 2.2 minutes.

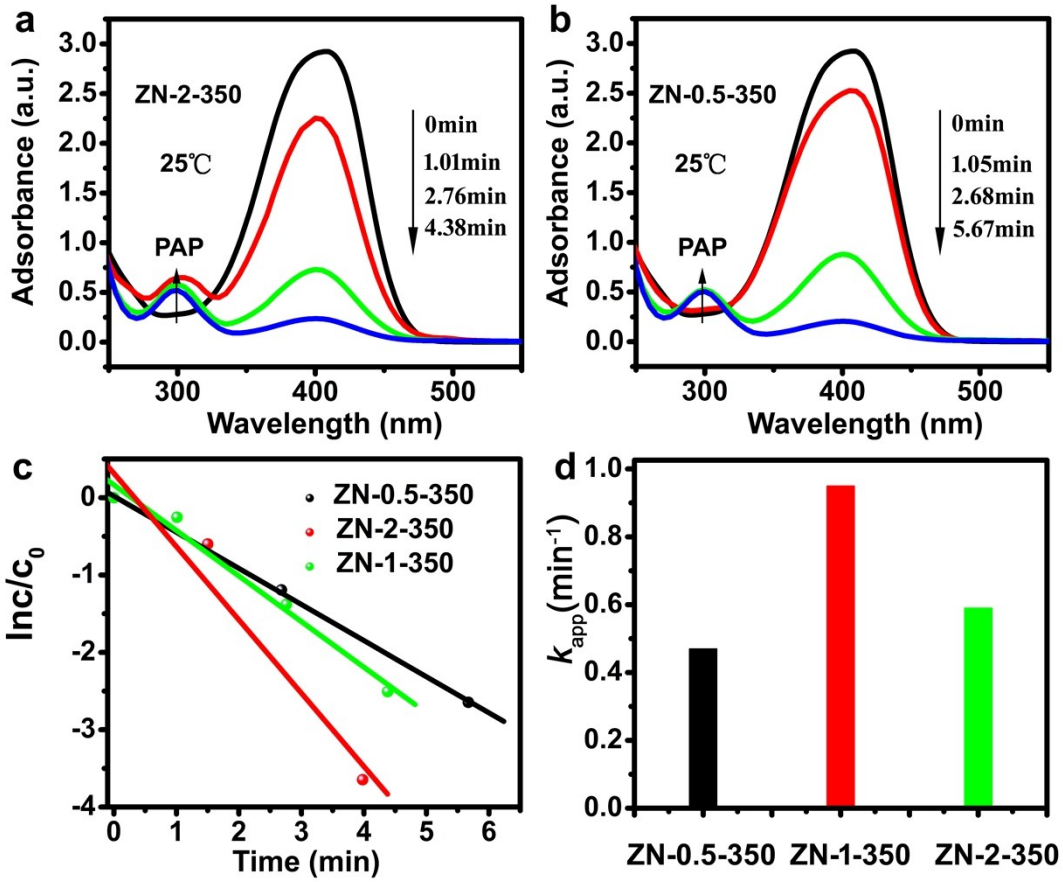

Figure S11. a-b) UV–vis absorption spectra of p-NP catalyzed by ZN-2-350, ZN-0.5-350. c) Pseudo-first-order plot of ln (C/C_0) against reaction time on ZN-0.5-350, ZN-1-350 and ZN-2-350 at 25°C. d) k_{app} of different catalysts at 25°C.

Figure S11a and b show UV-vis absorption spectra of the solution of PNP in the presence of Ni_3N-Co_3N with different Co/Ni ratio at a certain time interval. This can be almost completed in 3.98 min, 4.38 min and 5.67 min on ZN-0.5-350, ZN-1-350 and ZN-2-350. We can see that all Ni_3N-Co_3N show better performance for the conversion than ZIF-67-350 and Ni_3N derived from $Ni(OH)_2$ and the ZN-1-350 is the best one. Figure S11c shows the plot of $\ln(C/C_0)$ against reaction time for the hydrogenation of PNP over different catalysts. The rate constants of ZN-0.5-350, ZN-1-350, ZN-2-350 were 0.47, 0.95, and 0.59 min^{-1}, respectively. So, we can conclude that ZN-1-350 exhibited good catalytic activity, verifying that the suitable ratio is essential to give optimized performance.

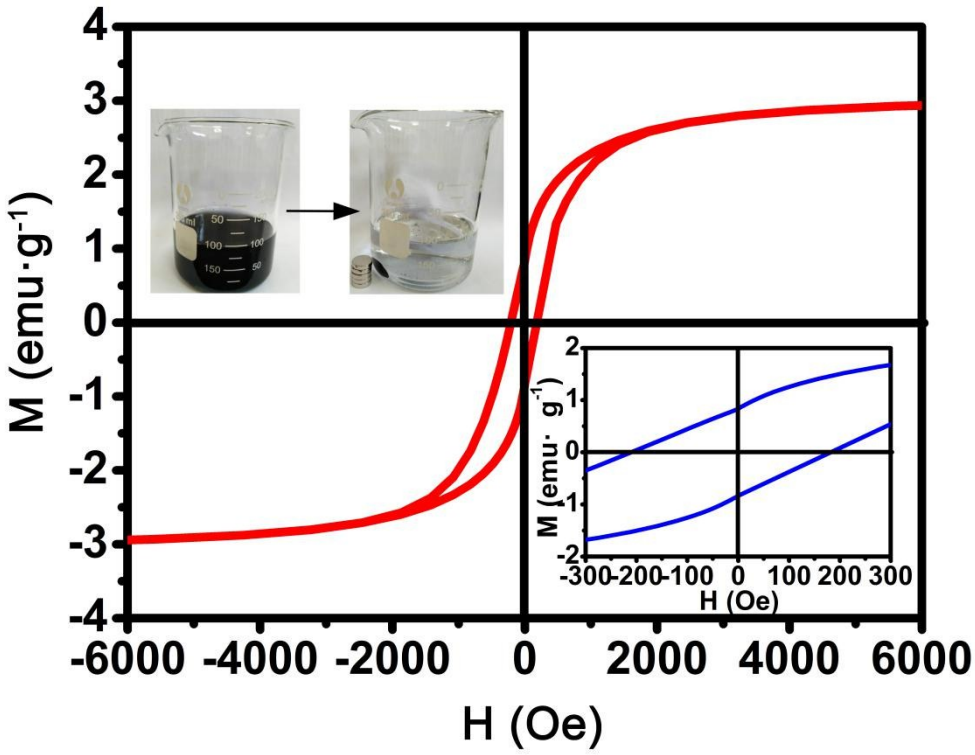

Figure S12. Magnetic hysteresis loop of 2-D Ni_3N-Co_3N catalyst at the temperature of 300K. The inset shows the enlargement of M–H loop at low magnetic field and the illustration of magnetic separation by an external magnet.

The magnetic hysteresis of Ni_3N-Co_3N was measured by a vibrating sample magnetometer at 300 K in the applied magnetic field sweeping from −6000Oe to +6000Oe. As shown in Figure S12, the typical hysteresis loop of Ni_3N-Co_3N in its magnetic behavior shows the soft magnetic nature. The saturation magnetization value of Ni_3N-Co_3N was found at 2.9 emu/g, whereas the coercivity and retentivity values were 208.7 kOe and 0.99 emu/g, respectively. This suggests that Ni_3N-Co_3N catalyst is sufficient enough to be easily separated from the dispersion system under an external magnetic field (see the left insert of Figure S12).

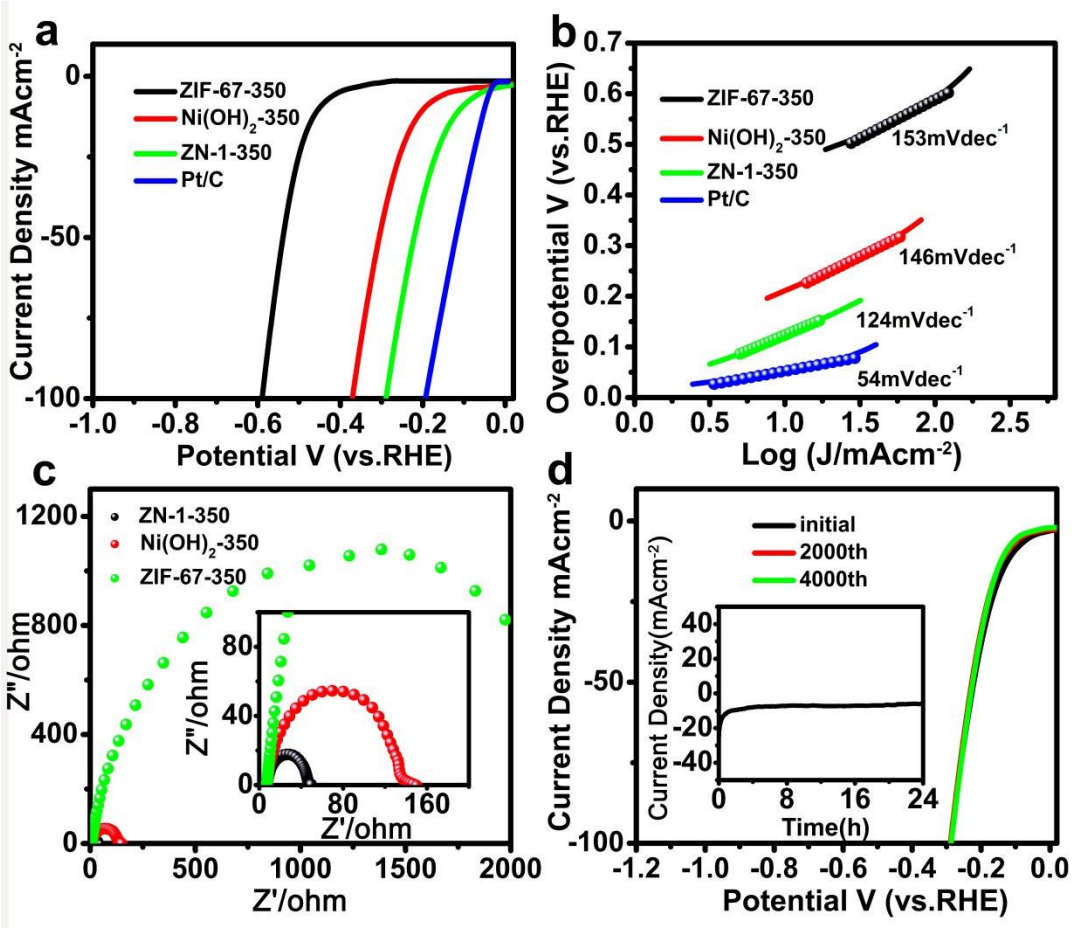

Figure S13. a) Polarization curves for ZIF-67-350, $Ni(OH)_2$-350, ZN-1-350 and Pt/C in 1M KOH with a scan rate of 5 mVs^{-1}. b) Tafel plots for ZIF-67-350, $Ni(OH)_2$-350, ZN-1-350 and Pt/C. c) Nyquist plots of ZIF-67-350, $Ni(OH)_2$-350, and ZN-1-350. The inset in (c) is the Nyquist plots for the high frequency region. d) Polarization data for the ZN-1-350 sample in 1M KOH initially and after 2000, and 4000 CV sweeps between -1000 and -1800mV vs RHE. The inset in (d) is the time dependence of the current density for ZN-1-350 under the temporal evolution of the potential required to maintain 10 mA cm^{-2} for 24h.

Figure S13a shows the polarization curves without iR correction. For comparison, 2-D Ni_3N-Co_3N, Ni_3N, ZIF-67-350 and commercial Pt/C catalyst were investigated under identical conditions. As expected, the Pt/C catalyst shows superior HER activity with negligible overpotential. The ZIF-67-350 was almost no obvious electrocatalytic activity. At the same time, $Ni(OH)_2$-350 (Ni_3N) also showed the poor activity. It is pleasing that the 2-D Ni_3N-Co_3N provides high catalytic activity. The

onset overpotential is about 43 mV, and the potential is about 109 mV to reach a current density of 10 $mAcm^{-2}$ (j_{10}). The Ni_3N derived from $Ni(OH)_2$ has an onset overpotential of 84 mV and j_{10} of 198 mV. Figure S13b presents the Tafel slopes of the samples derived from the polarization curves. The 2-D Ni_3N-Co_3N shows a Tafel slope of 126 ($mVdec^{-1}$), which is smaller than both $Ni(OH)_2$-350 (146 $mVdec^{-1}$) and ZIF-67-350 (153 mV dec^{-1}). The Tafel slope is determined by the rate limiting step associated with the catalyst reaction process, which indicating a HER route following the Volmer mechanismin in basic medium.[16] Electrochemical impedance spectroscopy (EIS) technique was carried out to gain further insight into the nature of catalytic activity. Figure S13c shows the Nyquist plots over as-prepared materials. The ZN-1-350 shows the fastest electrocatalytic faradaic process, implying its superior HER kinetics. The long-term durability of the Ni_3N-Co_3N toward HER was further examined using carbon rod as the counter electrode. After continuous CV scanning for 2000 cycles and 4000 cycles in 1 M KOH with a scan rate of 100 mVs^{-1}, the polarization curve showed negligible loss of current density compared with the original one, suggesting the good stability of 2-D Ni_3N-Co_3N in the long term electrochemical process. Furthermore, the long-term stability of 2-D Ni_3N-Co_3N was also evaluated by chronoamperometry. The catalyst was able to maintain its activity at least 24 h.

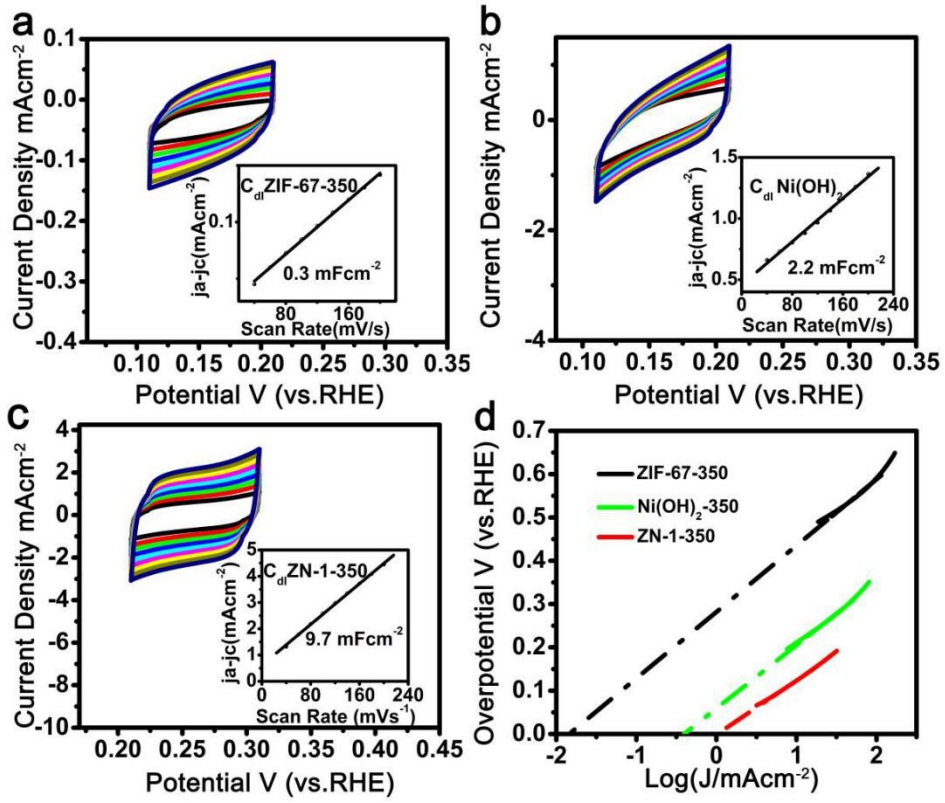

Figure S14. a-c) CVs for ZIF-67-350, $Ni(OH)_2$-350, ZN-1-350 with different rates from 40 to 200 mVs^{-1}. The inset in (a-c) is the capacitive current at 0.21 V as a function of scan rate for ZIF-67-350(j_0= ja-jc), $Ni(OH)_2$-350(j_0= ja-jc), ZN-1-350(j_0= ja-jc). d) Exchange current density of ZIF-67-350, $Ni(OH)_2$-350, ZN-1-350 composites.

The electrochemical surface area (ECSAs), which is the ratio of the electric double layer capacitance (C_{dl}), was used to further evaluate the catalytic properties. Based on the cyclic voltammograms (CVs) in the region of 0.2 V and 0.3 V, where the current response is only due to the charging of the double layer, the capacitances of 2-D Ni_3N-Co_3N, Ni_3N, ZIF-67-350 are calculated to be 9.7, 2.2, and 0.3 mF cm^{-2} respectively. The 2-D Ni_3N-Co_3N shows highest capacitance, revealing more catalytic active sites in 2-D Ni_3N-Co_3N. The exchange current density values of ZN-1-350 (2-D Ni_3N-Co_3N), $Ni(OH)_2$-350, ZIF-67-350 are 1.03, 0.39, 0.014 mA cm^{-2} (Figure S14d). The test further proves that ZN-1-350 has the large surface area, fast electron transmission, and favorable HER kinetic.[16]

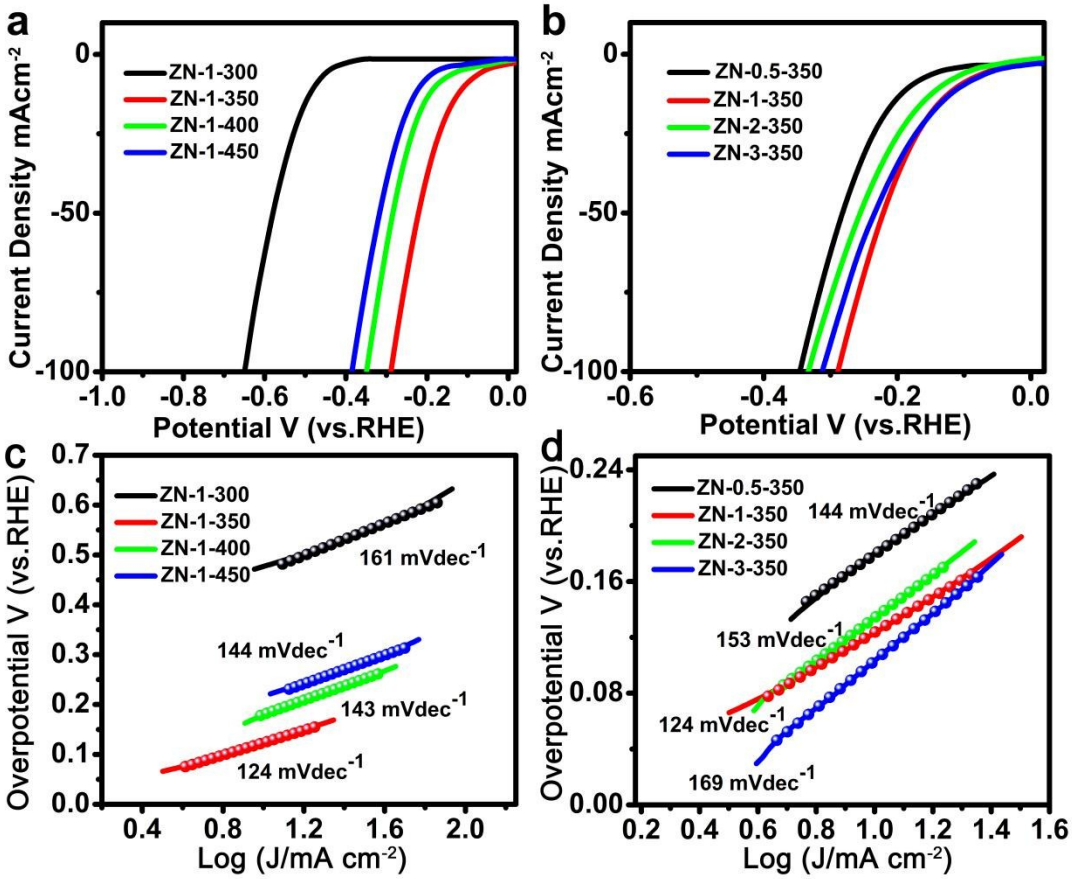

Figure S15. a) Polarization data for ZIF-67/$Ni(OH)_2$ calcined in different temperatures. b) Polarization data for different ratio ZIF-67/$Ni(OH)_2$ calcined at 350°C. c) Tafel plots for ZN-1-300, ZN-1-350, ZN-1-400, ZN-1-450. d) Tafel plots for ZN-0.5-350, ZN-1-350, ZN-2-350, ZN-3-350.

The polarization curves of ZN-1 at different calcining temperatures are shown in Figure S15a. The polarization curves for samples derived from the precursor with different ratio Co/Ni calcined at 350°C are shown in Figure S15b. The ZN-1-350 shows the best electrocatalytic activity. The good activity is relative with the sheet-like pore structure, which helps to expose more active centers. The presence of a pore structure allows the electrolyte to easily diffuse through the interface of the working electrode, therefore increasing current density and conversion efficiency.

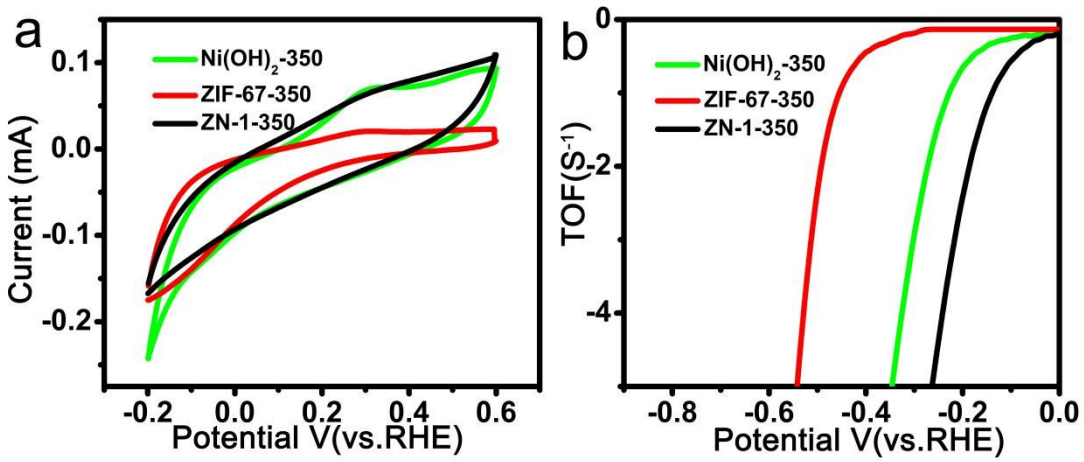

Figure S16. a) CVs of $Ni(OH)_2$-350, ZIF-67-350, ZN-1-350 in 1 M PBS with a scan rate of 50 mVs^{-1}. b) Calculated TOF for $Ni(OH)_2$-350, ZIF-67-350, ZN-1-350 in 1 M KOH.

To better evaluate the performance of the catalyst, the turnover frequency (TOF) of HER normalized to the number of active sites was estimated as shown in Figure S15. The CV curves are in the region of -0.2 to 0.6 V vs RHE for ZN-1-350 in 1 M phosphate buffer solution (PBS). The ZN-1-350 also has the highest TOF value of $0.563s^{-1}$ per site at overpotential of 100 mV, which is larger than that of Ni_3N ($0.253s^{-1}$) and ZIF-67-350 ($0.135s^{-1}$).

Table S1 The samples and their corresponding synthesis parameters

molar ratio $Co(NO_3)_2$:$Ni(OH)_2$	Starting material	Heating atmosphere	Heating temperature (℃)	Heating Time (h)	Final samples
1:3	ZN-1	NH_3	300	3h	ZN-1-300
1:3	ZN-1	NH_3	350	3h	ZN-1-350
1:3	ZN-1	NH_3	400	3h	ZN-1-400
1:3	ZN-1	NH_3	450	3h	ZN-1-450
3:3	ZN-3	NH_3	350	3h	ZN-3-350
2:3	ZN-2	NH_3	350	3h	ZN-2-350
0.5:3	ZN-0.5	NH_3	350	3h	ZN-0.5-350

The samples and their corresponding synthesis parameters

Physical mixing ZIF-67:$Ni(OH)_2$	Starting material	Heating atmosphere	Heating temperature (℃)	Heating Time (h)	Final samples
2:1	20mgZIF-67/10mg $Ni(OH)_2$	NH_3	350	3h	20mgZIF-67/10mg $Ni(OH)_2$-350
1:2	20mg$Ni(OH)_2$/10mg ZIF-67	NH_3	350	3h	20mg $Ni(OH)_2$/10mg ZIF-67-350

Table S2 Rate constants of the reduction of p-nitrophenol to p-aminophenol by metal catalysts

sample	p-NP (mM)	p-NP solution volume (mL)	Rate constant (min^{-1})	Time (min)	Reaction condition	Ref.
ZN-1-350	0.3	80	0.93	3.98	25°C	This work
$Ni_{0.22}$/CB	0.5	50	0.597	9	30°C	17
Ni-Ca-Al_2O_3	0.3	80	0.17	18	25°C	18
Ag/TiO_2	0.166	20	0.6	4.67	25°C	19
Ni Co alloy	0.03	10	0.07	30	20°C	20
Ag/PAN	0.13	30	0.085	70	R.T.	21
Pt-Au-PDA/RGO	0.1	2.7	0.575	5	R.T.	22
CNFs/AgNPs	0.12	30	0.372	8	25°C	23
Ag-NP/C	0.05	2.8	0.01	25	R.T.	24
Au/g-C_3N_4	0.07	50	0.356	8	25°C	25

Table S3 The performance of various catalysts for HER

Samples	η10 （mV）	Tafel slope (mV dec^{-1})	Exchange current j_0 (mA cm^{-2})
ZN-1-350	109	124	1.03
$Ni(OH)_2$-350	198	146	0.39
ZIF-67-350	453	153	0.014
Pt/C	50	54	-
ZN-1-300	477	161	-
ZN-1-400	179	143	-
ZN-1-450	217	144	-
ZN-0.5-350	181	144	-
ZN-2-350	135	124	
ZN-3-350	104	169	

References

1 W. Sun, X. Rui, J. Zhu, L. Yu, Y. Zhang, Z. Xu, S. Madhavi and Q. Yan, *Journal of Power Sources*, 2015, **274**, 755.

2 J. Feng, Q. Wang, D. Fan, L. Ma, D. Jiang, J. Xie and J. Zhu, *Applied Surface Science*, 2016, **382**, 135.

3 Y. Qu, M. Yang, J. Chai, Z. Tang, M. Shao, C. Tat Kwok, M. Yang, Z. Wang, D. Chua, S. Wang, Z. Lu and H.Pan., *ACS Appl. Mater. Interfaces,* 2017, **9**, 5959.

4 Y. Kyung Jo, M. Kim, X. Jin, I. Young Kim, J. Lim, N. Lee, Y. Kyu Hwang, J. Chang, H. Kim and S. Hwang, *Chem. Mater.*, 2017, **29**, 1028.

5 L. Kong, Z. Ren, S. Du, J. Wu and H. Fu, *Chem. Commun.*, 2014, **50**, 4921.

6 Y. Xu, W. Tu, B. Zhang, S. Yin, Y. Huang, M. Kraft and R. Xu, *Adv. Mater.*, 2017, 1605957.

7 C. Zhu, A. Wang, W. Xiao, D. Chao, X. Zhang, N. Huy Tiep, S. Chen, J. Kang, X. Wang, J. Ding, J. Wang, H. Zhang and H. Fan, *Adv. Mater*., 2018, 1705516.

8 R. K. Vishnu Prataap and S. Mohan, *Chem. Commun*., 2017, **53**, 3365.

9 K. Xu, P. Chen, X. Li, Y. Tong, H. Ding, X. Wu, W. Chu, Z. Peng, C. Wu and Yi Xie, *J. Am. Chem. Soc*., 2015, **137**, 4119.

10 P. Chen, K. Xu, Y. Tong, X. Li, S. Tao, Z. Fang, W. Chu, X. Wu and C. Wu, *Inorg. Chem. Front*., 2016, **3**, 236.

11 X. Li, C. Zeng, J. Jiang and L. Ai, *J. Mater. Chem. A*, 2016, **4**, 7476.

12 S. Deng, N. Chen, D. Deng, Y. Li, X. Xing and Y. Wang, *Ceramics International*, 2015, **41**, 11004.

13 C. Ray, S. Chan Lee, B. Jin, A. Kundu, J. Hyeok Park and S. Chan Jun, *J. Mater. Chem. A*, 2018, **6**, 4466.

14 F. Xi, X. Cao, F. Qu, A. M. Asiri and X. Sun., *Sensors and Actuators B*, 2018, **255**, 1254.

15 D. Gao, J. Zhang, T. Wang, W. Xiao, K. Tao, D. Xue and J. Ding, *J. Mater. Chem. A*, 2016, **4**, 17363.

16 J. Wang, F. Xu, H. Jin, Y. Chen and Y. Wang, *Adv. Mater*., 2017, **29**, 1605838.

17 J. Xia , G. He, L. Zhang, X. Sun and X. Wang, *Appl. Catal. B: Environ*., 2016, **180**, 408.

18 J. Feng, Q. Wang, D. Fan, L. Ma, D. Jiang, J. Xie and J. Zhu, *Applied Surface Science*, 2016, **382**, 135.

19 Y. Gu, Y. Jiao, X. Zhou, A. Wu , B. Buhe and H. Fu, *NanoResearch*, 2018, **11**, 126.

20 H. Chen, M. Yang, S. Tao and G.Chen, *Appl. Catal. B: Environ*., 2016, **198**, 74.

21 S. Gao, Z. Zhang, K. Liu and B. Dong, *Applied Catalysis B: Environmental*, 2016, **188**, 245.

22 W. Ye, J. Yu, Y. Zhou, D. Gao, D. Wang, C. Wang and D. Xue, *Applied Catalysis B: Environmental*, 2016, **181**, 371.

23 P. Zhang, C. Shao, Z. Zhang, M. Zhang, J. Mu, Z. Guo and Y. Liu, *Nanoscale*, 2011, **3**, 3357.

24 S. Tang, S. Vongehr and X. Meng, *J. Phys. Chem. C*, 2010, **114**, 977.

25 Y. Fu, T. Huang, B. Jia, J. Zhu and X. Wang, *Applied Catalysis B: Environmental*,

2017, **202**, 430.